

Contents lists available at ScienceDirect

# International Journal of Plasticity

journal homepage: www.elsevier.com/locate/ijplas



# An experimental study of the mechanical behavior of rolled AZ31B magnesium alloy under combined axial-torsion loading



Luiz Carneiro, Qin Yu\*,1, Yanyao Jiang\*

University of Nevada, Reno, Department of Mechanical Engineering, NV, 89557, USA

ARTICLE INFO

Keywords:
Magnesium alloy
Multiaxial stress
Combined axial-torsion loading
Twinning

#### ABSTRACT

The mechanical behavior and microstructure at fracture of a rolled AZ31B magnesium alloy were experimentally investigated using tubular specimens subjected to combined axial-torsion loading with different ratios of the axial and shear stress components. The stress state influences the stress-strain responses. The equivalent stress-equivalent plastic strain curves under tensiontorsion loading show a sigmoidal shape and the peak value of the equivalent strain hardening rate increases as the ratio of the axial stress to the shear stress increases. Under compressiontorsion, the equivalent stress-equivalent plastic strain curves show a concave-down shape, and the equivalent strain hardening rate decreases at faster rates as the ratio of the axial stress to the shear stress increases. Among all the loading conditions investigated, pure tension and pure compression result in the highest strength, and torsion combined with a slight tension has the lowest strength. The trend of ductility is inversely proportional to the strength with respect to the influence of the combined axial-torsion loading. Detailed twinning structures reveal that extensive tension twins are induced under tension-torsion loading paths. Conversely, a combination of tension and compression twins is observed under compression-torsion loading due to the high Schmid factors of the compression twins resulted from the grains with favorable orientations. The significant effect of the stress state on the post-fracture texture is explained in terms of the twin variant favorability which is dominated by the crystal orientation relative to the orientation of the applied principal stresses. The experimental results are critical for the development and validation of constitutive models for magnesium alloys under multiaxial loading.

# 1. Introduction

Magnesium (Mg) alloys are light-weight structural materials with a high specific strength. However, the hexagonal closed packed (hcp) crystal structure of the materials has a limited number of slip systems at room temperature, leading to poor formability and low ductility (Pollock, 2010; Wu et al., 2018; Wu and Curtin, 2015). Typical slip systems in Mg include  $\langle a \rangle$  basal,  $\langle a \rangle$  prismatic, and  $\langle c + a \rangle$  pyramidal slips. Slips other than  $\langle a \rangle$  basal slip are, in general, difficult to activate due to their high critical resolved shear stresses (CRSSs) at room temperature (Agnew and Duygulu, 2005). To accommodate plastic deformation, twinning plays an important role as an additional deformation mechanism in Mg alloys (Yoo, 1981). Twinning in Mg can occur on the  $\{10\overline{1}2\}$  plane to allow extension along the c-axis (i.e. tension twinning) or on the  $\{10\overline{1}1\}$  plane to accommodate c-axis contraction (i.e. compression twin). Because of

<sup>\*</sup> Corresponding authors.

E-mail addresses: qin.yu.unr@gmail.com (Q. Yu), yjiang@unr.edu (Y. Jiang).

Current address: Materials Sciences Division, Lawrence Berkeley National Laboratory, Berkeley, CA, 94720, USA.

the crystal lattice rotations associated with twinning, strong textures are usually resulted in wrought Mg alloys subsequent to material processing. For instance, hot rolling produces a strong basal texture in the Mg alloy where the grains orient predominantly with their *c*-axes parallel to the normal (or thickness) direction (ND) (Khan et al., 2011).

The stress-strain response and the associated deformation microstructure of Mg alloys under monotonic tension and monotonic compression have been extensively studied. Taking the rolled Mg alloys for example, the strong basal texture results in considerable anisotropic mechanical properties due to the polar nature of the twinning activities (Kelley and Hosford, 1968; Kurukuri et al., 2014; Lou et al., 2007; Tucker et al., 2009). Specifically, basal slip and tension twinning accommodate the plastic deformation in the rolled Mg alloys under tension along the ND (Carneiro et al., 2021b), whereas basal slip and  $\langle c + a \rangle$  pyramidal slip are dominant under compression parallel to the ND (Xi et al., 2018). Additionally, the strain hardening behavior in Mg alloys subjected to twinning-favorable loading is significantly different from that underlying slip-dominated deformation (Knezevic et al., 2010). For instance, the stress-strain curve under twinning-dominated deformation displays a characteristic sigmoidal shape, whereas slip-dominated deformation results in a common concave-down curve with monotonically decreasing strain hardening rates (Barnett, 2007a, 2007b; Kelley and Hosford, 1968; Lou et al., 2007; Tucker et al., 2009).

Studies on the deformation of Mg alloys under uniaxial loading are fundamentally important. However, the stress state in the materials of engineering components is often multiaxial, either due to the specific component geometry, such as notched components, or due to the nature of the service loads, such as automotive shafts subjected to combined torsion and bending. Due to the polar nature of twinning and interactions of slips and twinning, plastic deformation of Mg alloys cannot be described by the plasticity models for conventional metals. Unlike other metals, very limited experimental studies have been conducted on Mg alloys under multiaxial stress states. Experimental work has been done using cruciform specimens under biaxial in-plane loading (Abedini et al., 2018; Alkan et al., 2020; Andar et al., 2012; Banabic and Hußnätter, 2009; Cheng et al., 2020; Steglich et al., 2012), tubular specimens under combined internal pressure and axial load (Thomsen and Doen, 1944; Tomlinson et al., 2013), plate specimens under biaxial tension realized by hydraulic bulge or flat punch tests (Chino et al., 2009; Kim et al., 2012; Steglich et al., 2012; Yoshida, 2015), and specimens specially designed to induce shear-tension or shear-compression using conventional uniaxial testing machines (Dorogoy et al., 2016, 2015, 2002; Pan et al., 2016; Wang et al., 2020; Yang et al., 2019). It has been shown that the strength and ductility of the Mg alloys are significantly affected by the multiaxial stress state and loading paths due to distinct deformation mechanisms involved. For instance, the stress loci of AZ31B at different equivalent strains under multiaxial stresses deviate notably from the von Mises criteria for isotropic materials. This yielding anisotropy requires sophisticated functions to model the yield criteria (Andar et al., 2012; Banabic and Hußnätter, 2009; Cazacu and Barlat, 2004; Iftikhar and Khan, 2021; Kabirian and Khan, 2015; Mohr et al., 2013; Wang et al., 2020). Fundamentally, the yielding anisotropy in Mg alloys is partially correlated to the complex twinning behavior under multiaxial stresses (Cheng et al., 2020; Jiang et al., 2007b; Kim et al., 2012; Shi et al., 2017; Zhao et al., 2018). Kim et al. (2012) and Alkan et al. (2020) showed that both tension, compression, and compression-tension double twins may be activated under certain loading paths in a rolled AZ31 Mg alloy in biaxial tests. Jiang et al. (2007b) revealed that both tension and compression twins may be induced in different grains of an extruded AZ31 Mg alloy under ring hoop tension. Moreover, an earlier investigation revealed that pure shear stress state induces both tension and compression twins in a strong basal-textured AZ31B Mg alloy under free-end torsion (Carneiro et al., 2021b, 2021a).

With limited experiments, the twinning behavior under multiaxial stress states is not well understood. In addition, most of the multiaxial experiments were conducted using specially designed specimens where the stress and/or the strain were not directly measured. For instance, cruciform specimens do not allow for the direct measurement of the stresses without a secondary analysis (Lamkanfi et al., 2010). Neither the stress nor the strain was directly measured experimentally in the plate specimens under biaxial tension realized by hydraulic bulge tests (Chino et al., 2009; Kim et al., 2012). Additionally, axial-torsion experiments have been recently conducted using solid specimens (Shi et al., 2017; Wang et al., 2022), which is not ideal due to the non-uniform distributions of the shear stress and the shear strain along the radial direction of the specimen. In view of all the experimental methods, a thin-walled tubular specimen subjected to combined axial-torsion (and internal and external pressures) is the only choice that allows for a direct measurement of the stresses and the strains with acceptable accuracy. Few studies were conducted using thin-walled tubular specimens under combined axial-torsion loading for extruded Mg alloys under different combinations of the axial stress and the shear stress (Cheng and Krempl, 1991; Iftikhar and Khan, 2021; Inaba et al., 2008; Kabirian and Khan, 2015). Moreover, most of these studies considered only few axial-torsion loading paths or did not investigate the deformation microstructure in detail. For instance, Cheng and Krempl (1991) and Iftikhar and Khan (2021) investigated the yield surface of Mg alloys under combined axial-torsion loading employing several complex loading paths. Kabirian and Khan (2015) investigated the yield and stress loci of extruded AZ31 Mg alloy under combined axial-torsion loading at multiple equivalent strains employing four combined loading paths, Inaba et al. (2008) investigated the deformation behavior of the same material under combined axial-torsion at different temperatures. However, none of these studies involved a careful examination of fracture behavior or final microstructure under combined loading, in particular with regard to the twinning behavior. The current work aims to investigate the multiaxial stress state effect on the deformation, fracture, and microstructures (particularly twin structures) of a rolled AZ31B Mg alloy using thin-walled tubular specimens under various combinations of axial and torsion loads.

# 2. Experimental procedure

## 2.1. Material and specimen

The material used in this work is an AZ31B (Mg-3Al-1 Zn) Mg alloy in the form of a 76.2 mm thickness hot-rolled plate. The microstructure of the material in the as-received condition is presented in Fig. 1a. The microstructure was characterized in three

orthotropic planes with their normal orientation parallel to the rolling direction (RD), transverse direction (TD), and normal direction (ND) of the rolled plate. Electron backscatter diffraction (EBSD) scans show that the initial microstructure is composed by mostly equiaxed grains sized in an average of  $50 \, \mu \text{m}$  with no initial twins. The material displays a strong basal texture where most of the grains are oriented with the c-axes approximately parallel to the ND $\pm 15^{\circ}$  of the rolled plate, as shown in Fig. 1a.

Thin-walled tubular testing specimens were used for the combined axial-torsion experiments. The specimens were machined with their longitudinal axis parallel to the ND of the rolled plate, as illustrated in Fig. 1b. The specimen has a total length of 76.2 mm and a gage section of 26 mm with a 24 mm outer diameter and a 20 mm inner diameter. The outside surface of the gage section of each specimen was polished using *SiC* sandpapers with grit sizes from P400 to P1000 to remove any initial machining marks. For the monotonic tension and monotonic compression experiments, dog-bone shaped solid specimens were machined along the ND of the plate and have a gage section with 14 mm in length and 8 mm in diameter. The solid specimens were subjected to identical surface polishing procedures as the tubular specimens.

#### 2.2. Mechanical experiments

Mechanical experiments were conducted using a servo-hydraulic axial-torsion fatigue testing machine in ambient air. The machine has an axial load capacity of  $\pm 222$  kN and a torque capacity of  $\pm 2800$  Nm. For the monotonic tension and monotonic compression experiments, a clip-on extensometer with a gage length of 12.7 mm and a strain range of  $\pm 40\%$  was used for the strain measurement. For the combined axial-torsion experiments, a modified MTS clip-on extensometer with a gage length of 25.4 mm, an axial strain range of  $\pm 5\%/-3\%$ , and a shear strain range of  $\pm 3\%$  was used. The monotonic tension and monotonic compression experiments were conducted under displacement control at a strain rate of approximately  $5 \times 10^{-3}$  s  $^{-1}$ . The combined axial-torsion experiments were conducted under displacement and rotation angle control. For the combined loading experiments, different displacement and rotation angle rates were imposed for each specimen in order to characterize the mechanical response at different ratios of the axial stress/shear stresses, *i.e.*, different loading path angles ( $\alpha$ ), as illustrated in Fig. 1c. The displacement rates varied from 0.0167 mm·s<sup>-1</sup> to 0.055 mm·s<sup>-1</sup> and the rotation angle rates ranged from  $0.149 \cdot \bullet s^{-1}$  to  $0.415 \cdot \bullet s^{-1}$ . These displacement and rotation angle rates resulted in axial strain rates varying from  $4 \times 10^{-4}$  s  $^{-1}$  to  $1.5 \times 10^{-3}$  s  $^{-1}$  and shear strain rates varying from  $1.1 \times 10^{-3}$  s  $^{-1}$  to  $2.3 \times 10^{-3}$  s  $^{-1}$ , respectively. It should be noted that the first multiaxial experiment of the series was deliberately conducted under load and torque control. The purpose was to obtain an approximated relationship between the axial stress/displacement and shear stress/rotation angle for the axial and torsion channels, respectively. This combined compression-torsion test had a force rate of  $2.0 \times 10^{-3}$  and torque rate of  $2.0 \times 10^{-3}$  s  $^{-1}$  and a shear strain rate of  $2.0 \times 10^{-3}$  s  $^{-1}$ .

For the combined axial-torsion experiments, the extensometer was removed when the axial strain or the shear strain approached the measurement limit of the extensometer. After the experiment was completed and the specimen was unloaded, the residual axial plastic strain and shear plastic strain were measured, respectively, from the incremental displacement between the tangential lines and the change of the right angle between the tangential and axial lines which were engraved on the outer surface of the tubular specimen before mechanical testing. The axial and shear strains after the extensometer removal were extrapolated assuming a linear relationship

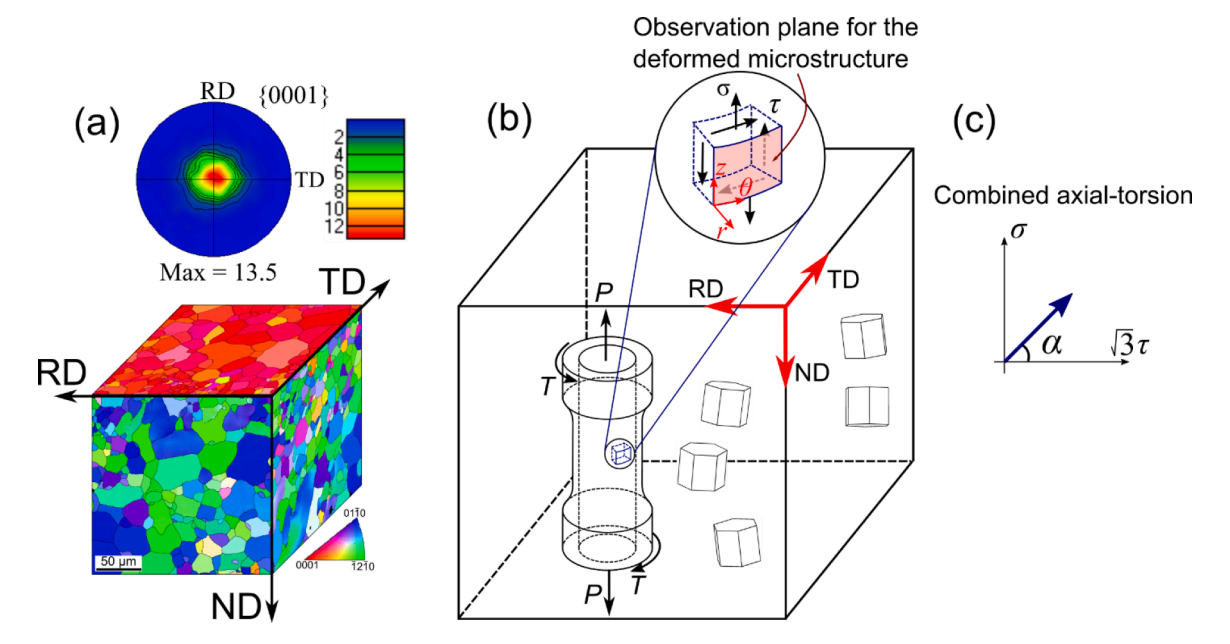


Fig. 1. Material, specimen, and loading paths. (a) Three-dimensional EBSD stereograph of the initial microstructure of the hot-rolled AZ31B Mg alloy. (b) Schematic illustration of the rolled plate with the tubular testing specimen oriented along the ND. (c) Labeling convention used for the combined axial-torsion loading path.

between the axial strain and the displacement measured by the linear variable displacement transducer (LVDT) as well as a linear relationship between the shear strain and the rotation angle measured by the rotary variable displacement transducer (RVDT). The axial stress ( $\sigma$ ) and the axial strain ( $\varepsilon$ ) reported are the true values calculated from the engineering stresses and strains. The shear stress ( $\tau$ ) and shear strain ( $\gamma$ ) reported are the values calculated on the mid-section of the tubular specimen assuming linear distributions of the shear stress and shear strain over the thickness of the specimen. To facilitate a comparison among the different loading paths, the equivalent stress ( $\overline{\sigma}$ ) and equivalent plastic strain ( $\overline{\varepsilon}_p$ ) are calculated as

$$\overline{\sigma} = \sqrt{\sigma^2 + 3\tau^2},\tag{1}$$

$$\overline{\varepsilon}_p = \sqrt{\varepsilon_p^2 + \left(\frac{1}{3}\right) \gamma_p^2},\tag{2}$$

where  $\sigma$  is the true axial stress,  $\tau$  is the shear stress,  $\varepsilon_p$  is the true axial plastic strain, and  $\gamma_p$  is the shear plastic strain. The axial plastic strain  $\varepsilon_p$  and the shear plastic strain  $\gamma_p$  are defined as follows:

$$\varepsilon_p = \varepsilon - \frac{\sigma}{E},$$
(3)

$$\gamma_{\rm p} = \gamma - \frac{\tau}{G_0},\tag{4}$$

where E is the elasticity modulus calculated considering non-linear elasticity and  $G_0$  is the shear modulus when the shear strain is zero. The elasticity modulus is defined as

$$E = E_0 \left( 1 - \frac{\sigma}{b} \right). \tag{5}$$

where  $E_0$  is the elasticity modulus when the stress is zero, and b is a material constant to account for the non-linear elasticity of the material. For the AZ31B Mg alloy used in the present investigation, b = 20,000 MPa provides a good description of the non-linear elasticity. The consideration of non-linear elasticity is based on the assumption that the elastic deformation is identical before microyielding under pure tension and pure compression (Dong et al., 2017). Also, the elasticity and shear moduli when the stress is zero ( $E_0$ ,  $G_0$ ) were measured individually for each combined test. The average moduli were calculated as  $E_0 = 48.9$  GPa and  $G_0 = 17.0$  GPa. Finally, it should be noticed that these definitions of equivalent stress and equivalent plastic strain are for isotropic materials and are adopted in the present work to facilitate discussions for the textured Mg alloy.

The loading path angle ( $\alpha$ ) is proportional to the ratio of the axial stress and the equivalent shear stress at fracture, as illustrated in Fig. 1c. This loading path angle is calculated for each experiment as

$$\alpha = \tan^{-1}\left(\frac{\sigma_f}{\sqrt{3}\tau_f}\right),\tag{6}$$

where  $\sigma_f$  are the axial and the shear stresses at fracture. This formulation of the loading path angle for multiaxial experiments is similar to what was proposed by Mohr et al. (2013), but using the equivalent shear stress in the denominator of Eq. (6) instead of the absolute shear stress. The axial and shear strain rates for each combined axial-torsion test were approximately designed to induce stress states that reflect axial-dominant, shear-dominant, and combined axial/shear loading paths. The combination of the axial and shear strain rates used for each specimen resulted in loading path angles of  $-72^{\circ}$ ,  $-56^{\circ}$ ,  $-44^{\circ}$ , and  $-33^{\circ}$  for the combined compression-torsion tests, and  $+17^{\circ}$ ,  $+49^{\circ}$ , and  $+70^{\circ}$  for the combined tension-torsion tests. Additionally, monotonic tension,  $\alpha=90^{\circ}$ , monotonic compression,  $\alpha=-90^{\circ}$ , and free-end torsion,  $\alpha=0^{\circ}$ , experiments were performed.

# 2.3. Microstructure characterization

The post-fracture microstructure under each loading path was examined by EBSD characterization. The EBSD samples were prepared from the tested specimens with the unit normal of the scan plane parallel to the radial direction (r). The vertical axis of the scan is the longitudinal direction (z) and the horizontal axis is the hoop direction ( $\theta$ ) in the sample local coordinate system ( $r\theta z$ ), as illustrated in Fig. 1b. The samples were cut from the gage section of the specimens away from the fracture surface and were mechanically ground using *SiC* sandpapers until the surface of the specimen were flattened and had a surface finish of P1200 grit size. The samples were then polished by vibratory polishing using aluminum oxide with particle size of 0.05  $\mu$ m and etched with 3% Nital for 5 s. The EBSD scans were taken in a Joel 7100 F field emission scanning electron microscope (SEM) equipped with an Oxford HKL Channel 5 instrument at an acceleration voltage of 20 kV. The working distance was 25 mm, the step size was 0.6  $\mu$ m, and the scan size was at 450  $\times$  450  $\mu$ m<sup>2</sup>.

#### 3. Results and discussion

#### 3.1. Stress-strain response

Some results from the stress-strain response obtained from the combined axial-torsion experiments are presented in Fig. 2. The strain paths are presented in the axial plastic strain  $(\varepsilon_p)$  – shear plastic strain  $(1/\sqrt{3})\gamma_p$  space (Fig. 2a) whereas the stress responses are plotted in the axial stress  $(\sigma)$  – shear stress  $(\sqrt{3}\tau)$  space (Fig. 2b). The experiments were conducted under displacement and rotation angle control and therefore, the measured strain paths within the gage section of the specimens are not exactly linear, as seen in Fig. 2a. The stress responses display relatively tortuous paths in the  $\sigma - \sqrt{3}\tau$  space for the combined loading paths, except for the loading path  $\alpha = -44^\circ$ , which was exceptionally conducted under load/torque control (Fig. 2b). Therefore, the loading path angle  $\alpha$  is not exactly constant during the experiment, and it should be reiterated that the value presented is taken at the moment of fracture.

The mechanical properties obtained from the combined loading experiments for the rolled AZ31B are summarized in Table 1. Listed in the table include the stresses, strains, and plastic strains after fracture for each loading path except for the loading path  $\alpha=-72^{\circ}$  where the experiment was terminated when buckling was detected within the gage section of the thin-walled tubular specimen. It should be noted that loading path  $\alpha=0^{\circ}$  (free-end torsion) presents considerable axial strain throughout deformation, as can be seen in Fig. 2a, which is a typical phenomenon of Swift effect (Swift, 1947). At fracture, the axial elongation of the pure torsion specimen reaches 3.5%, and it is mostly resulted from the misfit axial strain caused by tension twinning accompanying large deformation under free-end torsion on AZ31B Mg alloy (Carneiro et al., 2021a).

The axial stress-axial plastic strain curves and the shear stress-shear plastic strain curves for the AZ31B Mg alloy under combined axial-torsion loading are presented in Fig. 3. The shapes of the stress-strain curves are strongly dependent on the loading paths. Under monotonic tension along the ND of the rolled AZ31B ( $\alpha=90^\circ$ , Fig. 3a), the stress-strain curve displays a strong sigmoidal shape due to the profuse activation of tension twins (Carneiro et al., 2021b). Under free-end torsion ( $\alpha=0^\circ$ , Fig. 3b), the shear stress-shear strain curve displays a less, but noticeable, sigmoidal shape. This arises from the relatively low amount of tension twins activated under pure torsion as compared to pure tension (Carneiro et al., 2021b, 2021a). As the loading path angle ( $\alpha$ ) decreases from  $90^\circ$  to  $90^\circ$ , the stress-strain curves are featured by a less pronounced sigmoidal shape and the material displays a lower strain hardening rate as the loading mode becomes more torsion dominant. As a consequence, the axial stress at a given axial strain is lower when compared to pure tension. On the other hand, when the loading angle decreases from  $90^\circ$  to  $90^\circ$ , the shear stress-shear strain curves show a less pronounced sigmoidal shape as tension becomes less dominant (Fig. 3b). For instance, when  $\alpha=70^\circ$ , the shear stress decreases after yielding and subsequently increases at a high rate with increasing shear strain. The higher strain hardening rates are likely resulted from the hardening effects contributed by the twinning texture as well as the formation of twin boundaries, because tension twinning is favored under the tension-dominated loading paths (Carneiro et al., 2021b).

Fig. 3c shows the axial stress-axial plastic strain curves under combined compression-torsion and pure compression. The stress-strain curve under pure compression displays a concave-down shape, which is a typical dislocation slip-dominated deformation

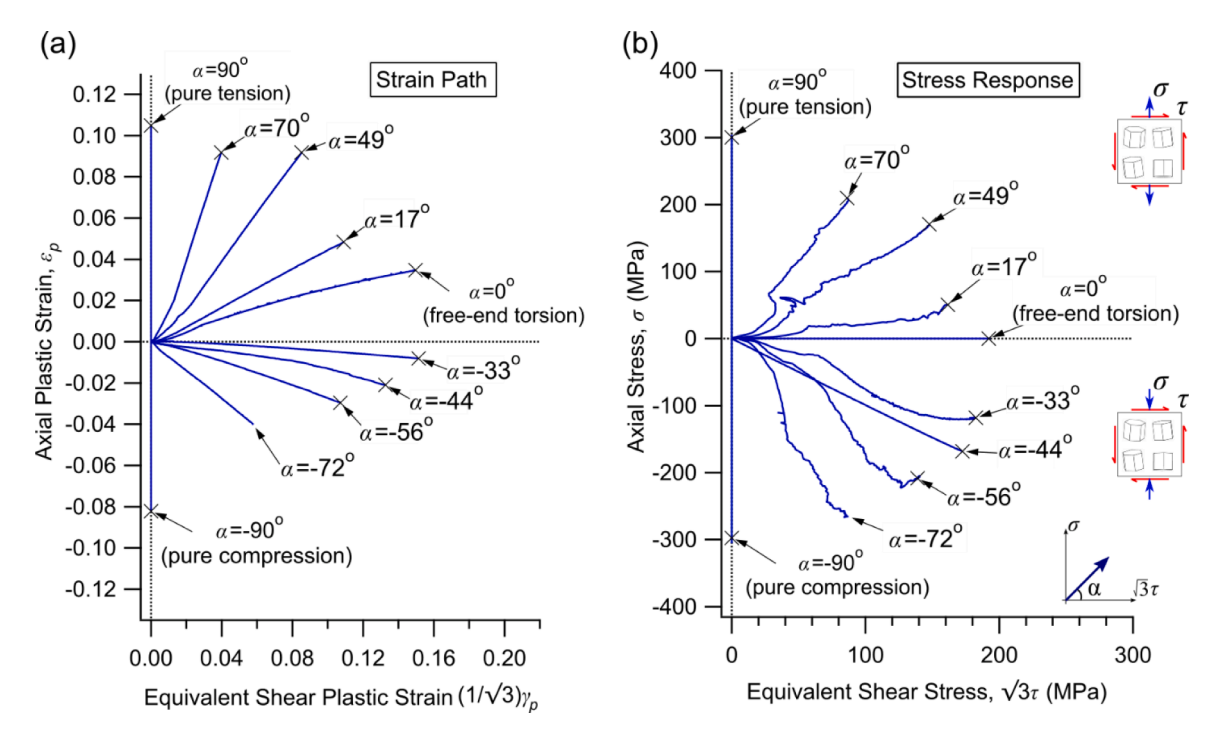


Fig. 2. (a) Measured strain paths and (b) the stress responses under combined axial-torsion loading. "X" denotes the moment of fracture.

Table 1
Summary of the uniaxial, free-end torsion, and combined axial-torsion experiments conducted on rolled AZ31B Mg alloy.

Strain path	Spec ID	α(°)	$\sigma_f(\mathrm{MPa})$	$arepsilon_f$	$arepsilon_{p,f}$	$\tau_f$ (MPa)	$\gamma_f$	$\gamma_{p,f}$
Monotonic compression	90S11	-90	-297.2	-0.088	-0.082	0.0	0.000	0.000
Compression-torsion	CT30*	-72	-265.2	-0.046	-0.040	50.4	0.103	0.100
	CT28	-56	-208.3	-0.034	-0.030	80.2	0.190	0.186
	CT24	-44	-168.3	-0.024	-0.021	99.6	0.236	0.230
	CT27	-33	-118.2	-0.010	-0.008	105.4	0.269	0.262
Pure torsion	CT18	0	0.0	0.035	0.035	110.9	0.266	0.259
Tension-torsion	CT25	17	50.4	0.050	0.048	93.3	0.194	0.189
	CT37	49	170.7	0.095	0.092	85.3	0.153	0.148
	CT26	70	217.5	0.099	0.092	49.7	0.056	0.069
Monotonic tension	90805	90	300.1	0.111	0.105	0.0	0.000	0.000

 $\alpha$ : loading path;  $\sigma_f$ : axial stress;  $\varepsilon_f$ : axial strain;  $\varepsilon_{pf}$ : axial plastic strain;  $\tau_f$ : shear stress;  $\gamma_f$ : shear strain;  $\gamma_{pf}$ : plastic shear strain. All the stress/strain values were obtained at the moment of fracture. \*Note: Stress/strain values for specimen CT30 were measured at the moment when buckling was detected.

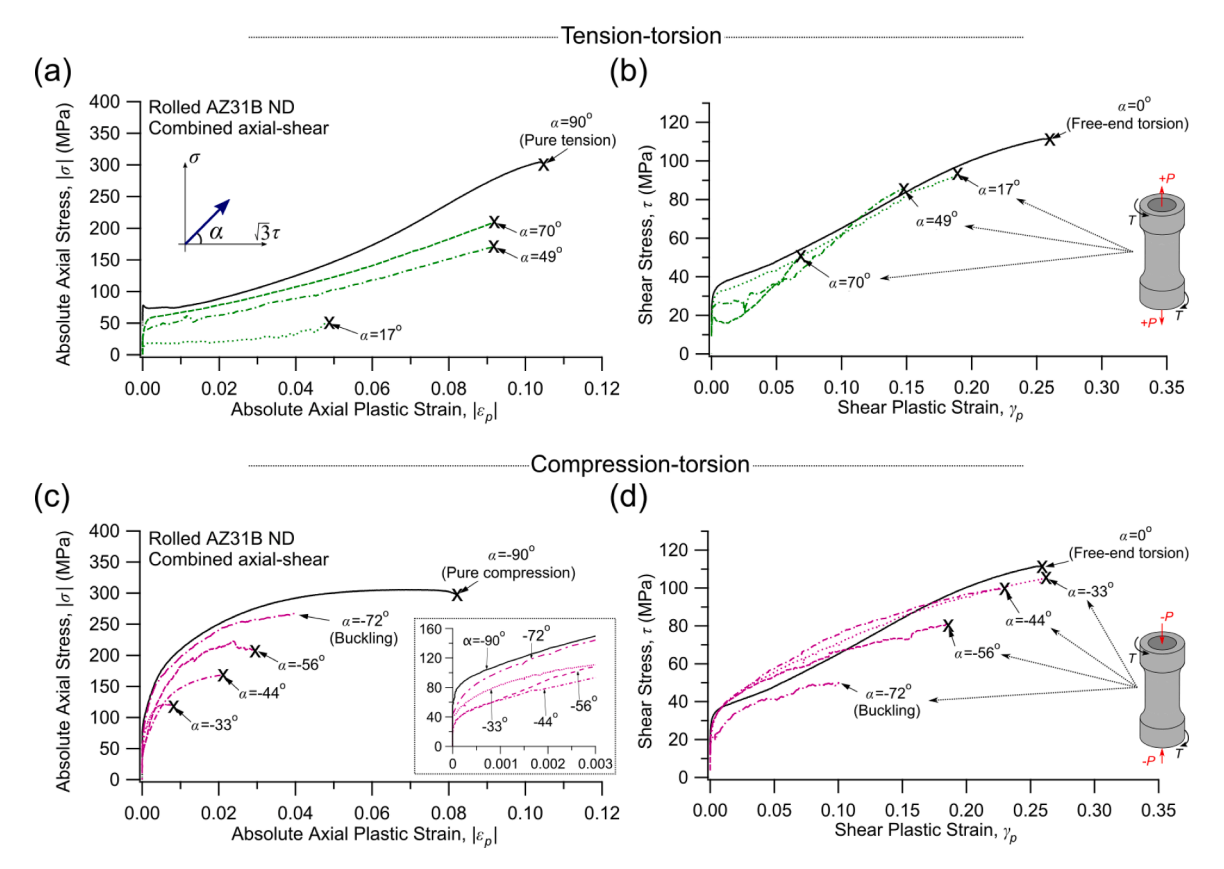


Fig. 3. Axial stress-axial plastic strain curves and shear stress-shear plastic strain curves of rolled AZ31B Mg alloy under (a, b) tension-torsion and under (c, d) compression-torsion loading paths. "X" denotes the moment of fracture.

(Jiang et al., 2008). This concave-down shape is regularly featured on the axial stress-strain curves under combined compression-torsion (Fig. 3c), indicating that twinning does not play a significant role on the plastic deformation under combined compression-torsion. However, the hardening rate decreases at faster rates as torsion becomes more dominant with the increase of the loading path angle  $\alpha$ . Consequently, the axial flow stress is measured at a lower level under combined compression-torsion than that under pure compression at an identical axial plastic strain. The shear stress-shear plastic strain curves also show a concave-down shape under compression-torsion for different loading paths, as shown in Fig. 3d. It is noted that this shape is significantly different from that under free-end torsion, where a sigmoidal shape is evident. As compression becomes dominant, *i.e.*,  $\alpha$  decreases, the hardening rate decreases at a faster rate, and the stress levels are lower at an identical shear plastic strain.

The Swift effect observed in the rolled AZ31B under free-end torsion plays a significant role on the axial stress response under

combined axial-torsion. As shown in Fig. 2a, free-end torsion induces an axial elongation of the specimen, which is mostly attributed to the twinning activity (Carneiro et al., 2021a, 2021b). When torsion is coupled with tension, the Swift effect-related axial strain occurs in the same direction as the applied axial stress. As a result, the axial deformation is facilitated, which decreases the axial flow stress and the hardening rate, as can be seen in the case of  $\alpha=17^\circ$  in (Fig. 3a). In a similar manner, the twinning behavior induced by the tensile-dominating loading path facilitates the shear deformation, thus reducing the required shear stress under tension-torsion loading  $\alpha=70^\circ$  (Fig. 3b). On the other hand, under compression-torsion, the applied compression stress and the torsion-induced axial strain are in opposite directions. Therefore, for the torsion-dominated compression-torsion path, such as  $\alpha=-33^\circ$ , the axial stress needs to overcome the Swift effect-related extension induced by torsion, which results in a higher yield stress and higher strain hardening rates at early stages of plastic deformation ( $\epsilon<0.3\%$ ,  $\gamma<13\%$ ) for the case of  $\alpha=-33^\circ$  than those observed in the cases of  $\alpha=-44^\circ$  and  $-56^\circ$  (see the inset in Fig. 3c). From intermediate to high strains ( $\epsilon>0.3\%$ ,  $\gamma>13\%$ ), the compressive flow stress decreases at relatively higher rates for the torsion-dominated path  $\alpha=-33^\circ$  This is possibly ascribed to the texture change caused by twinning that is induced by torsion at later stages of deformation. The detailed twinning behavior will be discussed in Section 3.2.

Fig. 4a presents the equivalent stress-equivalent plastic strain  $(\overline{\sigma} - \overline{\epsilon}_p)$  curves for the rolled AZ31B Mg alloy under monotonic tension, free-end torsion, and combined tension-torsion loading. The  $\overline{\sigma} - \overline{\epsilon}_p$  curves display a similar sigmoidal shape that is typical of twinning-dominated deformation (Jiang et al., 2007a; Lou et al., 2007). At an identical plastic strain, higher stress levels are observed as the loading path angle  $\alpha$  increases, *i.e.*, tension becomes more dominant. For instance, the equivalent stress at fracture is 169.3 MPa for  $\alpha = 17^{\circ}$ , 225.7 MPa for  $\alpha = 49^{\circ}$ , and 300.1 MPa for  $\alpha = 90^{\circ}$  (pure tension). The overall higher flow stresses for tension-dominant loading paths are resulted from the higher strain hardening rates after yielding.

To facilitate a comparison of the hardening behavior under different loading paths, the variation of the equivalent plastic modulus  $(d\overline{\sigma}/d\overline{e}_p)$  with the plastic strain is presented in Fig. 4b. The maximum hardening rates increases as tension becomes dominant, *i.e.*,  $\alpha$  increases. For instance, the plastic modulus reaches a maximum of 1.05 GPa for  $\alpha=17^{\circ}$ , 1.78 GPa for  $\alpha=49^{\circ}$ , and 3.60 GPa for  $\alpha=90^{\circ}$  (pure tension). The ductility of the AZ31B Mg alloy is also dependent on the loading path. The equivalent plastic strain at fracture is the highest when  $\alpha=0^{\circ}$  (free-end torsion), and decreases as  $\alpha$  increases. For instance, the equivalent plastic strain at fracture is 0.150 under  $\alpha=0^{\circ}$  (free-end torsion), 0.125 under  $\alpha=49^{\circ}$ , and 0.105 under  $\alpha=90^{\circ}$  (pure tension).

The equivalent stress-equivalent plastic strain  $(\bar{\sigma} - \bar{\epsilon}_p)$  curves and the equivalent plastic modulus-equivalent plastic strain  $(d\bar{\sigma}/d\bar{\epsilon}_p - \bar{\epsilon}_p)$  curves under combined compression-torsion loading are presented in Figs. 4c, d, respectively. As expected from the axial and shear stress-strain curves presented in Figs. 3c, d, the  $\bar{\sigma} - \bar{\epsilon}_p$  curves under combined compression-torsion display concave-down shapes. The yield and fracture stresses are higher as  $\alpha$  decreases, i.e. compression becomes dominant. For instance, the equivalent stress at fracture is 217.5 MPa for  $\alpha = -33^\circ$ , 241.0 MPa for  $\alpha = -44^\circ$ , and 297.2 MPa for  $\alpha = -90^\circ$  In an opposite fashion, the plastic strain at fracture shows a decreasing trend as  $\alpha$  decreases. The equivalent plastic strain at fracture is 0.152 under  $\alpha = -33^\circ$ , 0.134 under  $\alpha =$ 

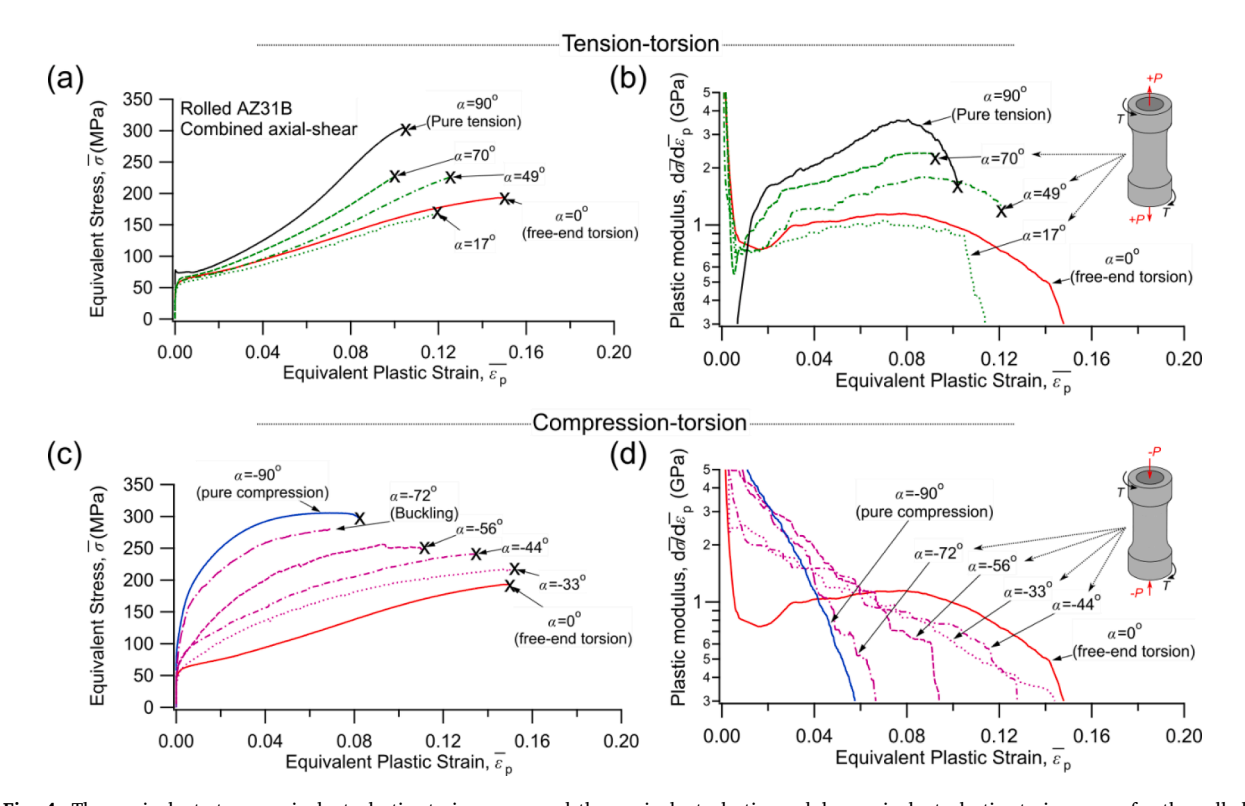


Fig. 4. The equivalent stress-equivalent plastic strain curves and the equivalent plastic modulus-equivalent plastic strain curves for the rolled AZ31B Mg alloy under (a, b) tension-torsion and under (c, d) compression-torsion combined loading. "X" mark denotes the moment of fracture.

44°, and 0.082 under  $\alpha = -90^{\circ}$  (pure compression).

Compared to torsion-dominated loading paths, the plastic modulus of a combined compression-torsion case is higher after yielding, and decreases at faster rates in later stages, as shown in the Fig. 4d. It should be noted that the equivalent plastic strain hardening behavior under free-end torsion ( $\alpha=0^{\circ}$ ) is different from those under combined compression-torsion. The plastic modulus  $d\overline{\sigma}/d\overline{\epsilon}_p$  of the former shows three distinct stages: i. sharp decrease, ii. subsequent increase, iii. gradual decrease, whereas combined compression-torsion loading induces a progressive decrease of  $d\overline{\sigma}/d\overline{\epsilon}_p$  all the way until fracture. Such behavior is an indication of a lower hardening effect caused by the suppression of twinning under combined compression-torsion, which is in contrast to the case under free-end torsion, where the three stages of strain hardening are associated with the formation of tension twins during deformation (Carneiro et al., 2021b).

## 3.2. Yield/fracture stress loci

The stress loci for the AZ31B Mg alloy at equivalent plastic strains of 0.2% and 1.0% are shown in Fig. 5. The stresses at fracture, which are shown in Fig. 2b, are also reproduced in Fig. 5 to facilitate a discussion. According to the von Mises criterion, the yield

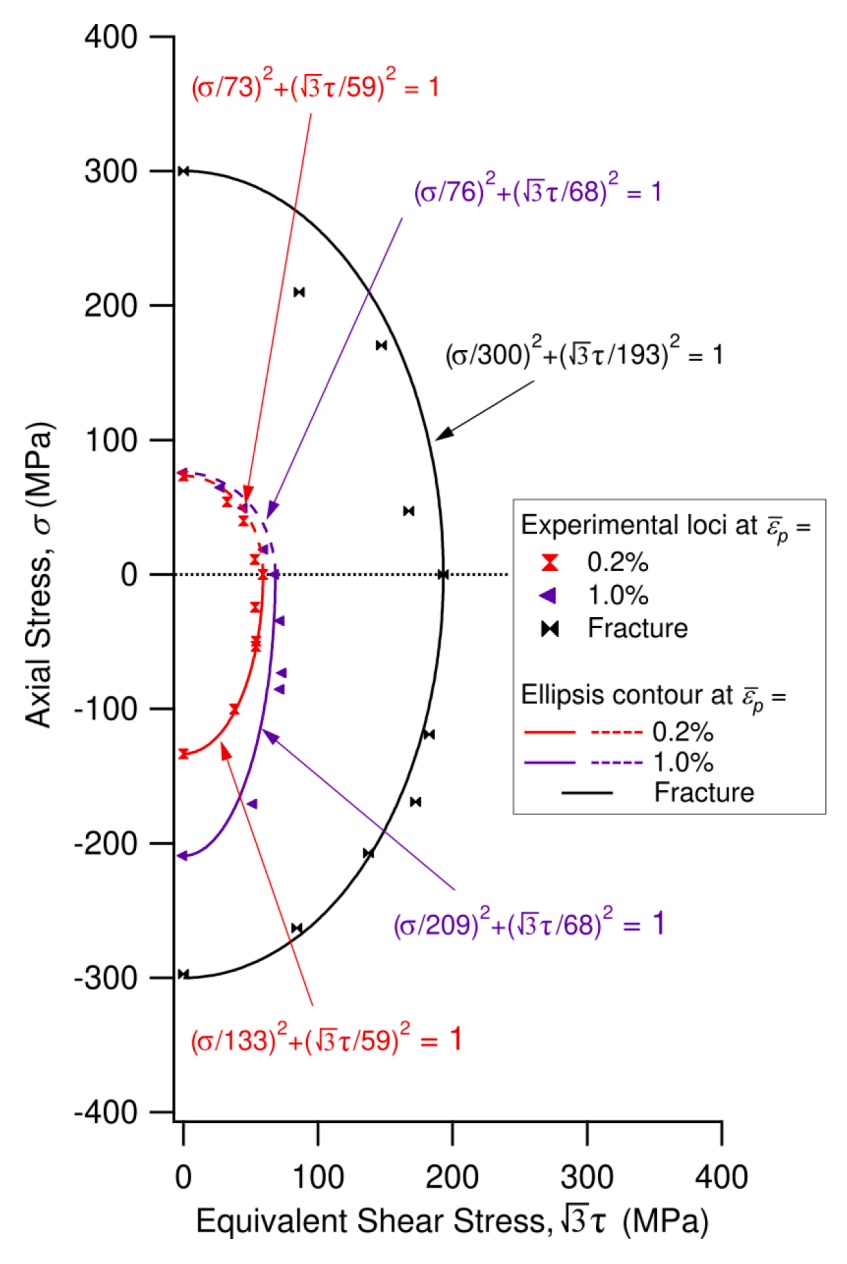


Fig. 5. Yield/fracture stress loci for the rolled AZ31B Mg alloy at the equivalent plastic strains of 0.2%, 1.0%, and at fracture.

surface of an isotropic material is represented by a circle in the  $\sigma - \sqrt{3}\tau$  space. For the rolled AZ31B Mg alloy, an ellipsis equation was used to represent the stress loci. The equation can be formulated as

$$\left(\frac{\sigma}{\sigma_{\alpha=-90^{\circ}}}\right)^{2} + \left(\frac{\sqrt{3}\tau}{\left(\sqrt{3}\tau\right)_{\alpha=0^{\circ}}}\right)^{2} = 1 \text{ If } -90^{\circ} < \alpha < 0^{\circ}$$

$$\left(\frac{\sigma}{\sigma_{\alpha=90^{\circ}}}\right)^{2} + \left(\frac{\sqrt{3}\tau}{\left(\sqrt{3}\tau\right)_{\alpha=0^{\circ}}}\right)^{2} = 1 \text{ If } 0^{\circ} < \alpha < 90^{\circ}$$
(7)

where  $\sigma_{a=-90^{\circ}}$ ,  $\sigma_{a=90^{\circ}}$ , and  $(\sqrt{3}\,\tau)_{a=0^{\circ}}$  are axial stress under pure compression, axial stress under pure tension, and equivalent shear

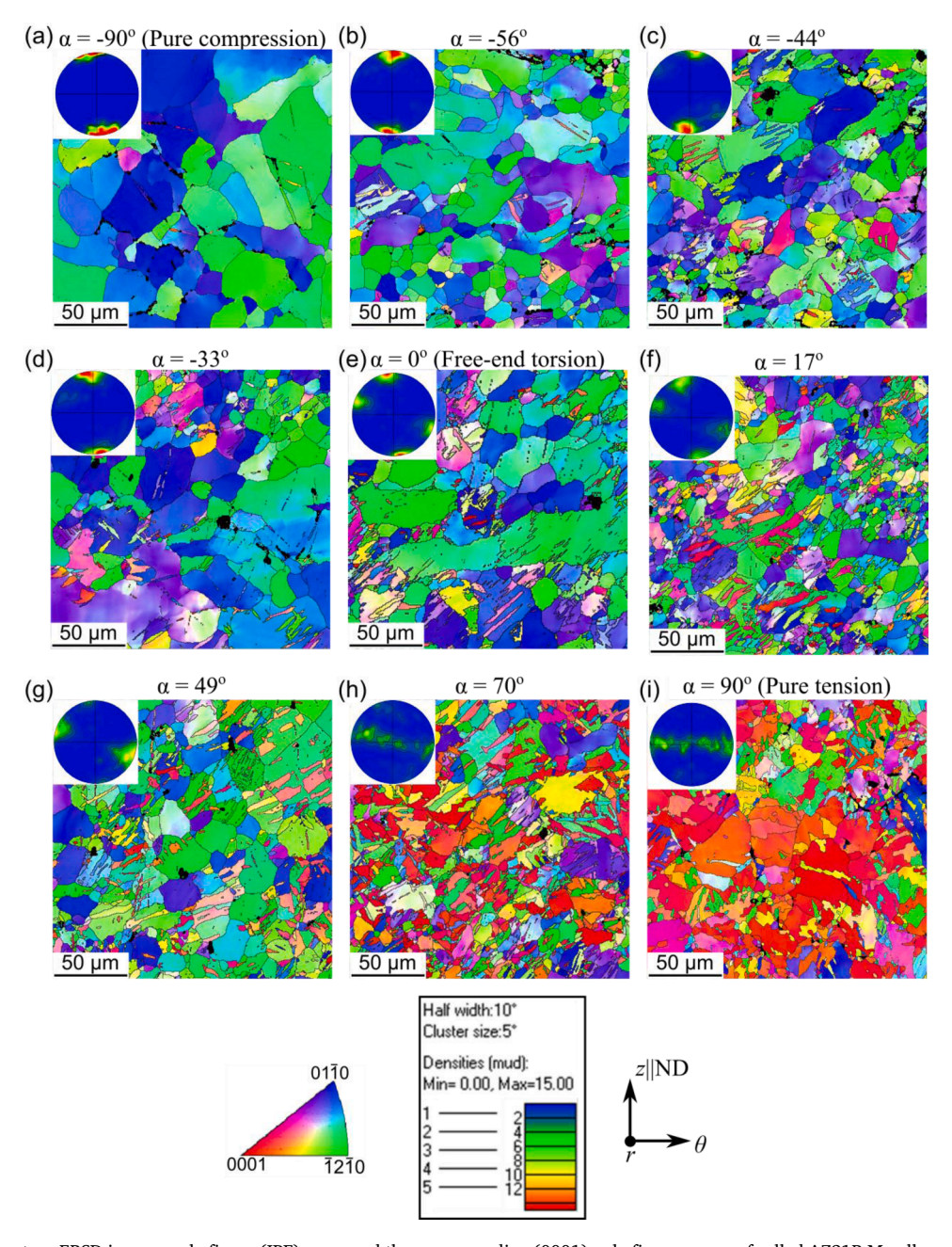


**Fig. 6.** Post-fracture EBSD inverse pole figure (IPF) maps and the corresponding (0001) pole figures maps of rolled AZ31B Mg alloy under different loading paths: (a)  $\alpha = -90^{\circ}$  (pure compression); (b)  $\alpha = -56^{\circ}$ ; (c)  $\alpha = -44^{\circ}$ ; (d)  $\alpha = -33^{\circ}$ ; (e)  $\alpha = 0^{\circ}$  (free-end torsion); (f)  $\alpha = 17^{\circ}$ ; (g)  $\alpha = 49^{\circ}$ ; (h)  $\alpha = 70^{\circ}$ ; (i)  $\alpha = 90^{\circ}$  (pure tension).

stress under free-end torsion at a given equivalent plastic strain level, respectively. Since the axial and shear stresses at fracture are almost identical under pure tension and pure compression, a single set of parameters can describe reasonably well the fracture stresses under both compression-torsion and tension-torsion, as shown by the black line in Fig. 5. This simplified representation describes well the fracture stress loci under compression-torsion, but slightly overestimates the fracture stress loci under tension-torsion, which is evidenced by the experimental loci being mostly inside the theoretical contour. At equivalent plastic strains of 0.2% and 1.0%, a clear difference is observed in the yield stress loci between pure compression and pure tension. Specifically, at  $\bar{\epsilon}_p = 0.2\%$ , the axial stress is 73 MPa under pure tension, while it is 133 MPa under pure compression. At  $\bar{\epsilon}_p = 1.0\%$ , the axial stress axial stress is 76 MPa under pure tension, while it is 209 MPa under pure compression. The use of two semi-ellipses taking the formulation of Eq. (7) gives a good description of the experimental results for the yield stress loci at the strains of  $\bar{\epsilon}_p = 0.2\%$  and 1.0%.

The different stress loci under tension-torsion and under compression-torsion are a result of the very distinct deformation mechanisms. When the Mg alloy is subjected to pure tension along the ND, tension twinning and basal slips accommodate most of the plastic deformation when  $\varepsilon_p < 4\%$  (Carneiro et al., 2021b), while under pure compression along the ND, tension twinning is unfavorable, and

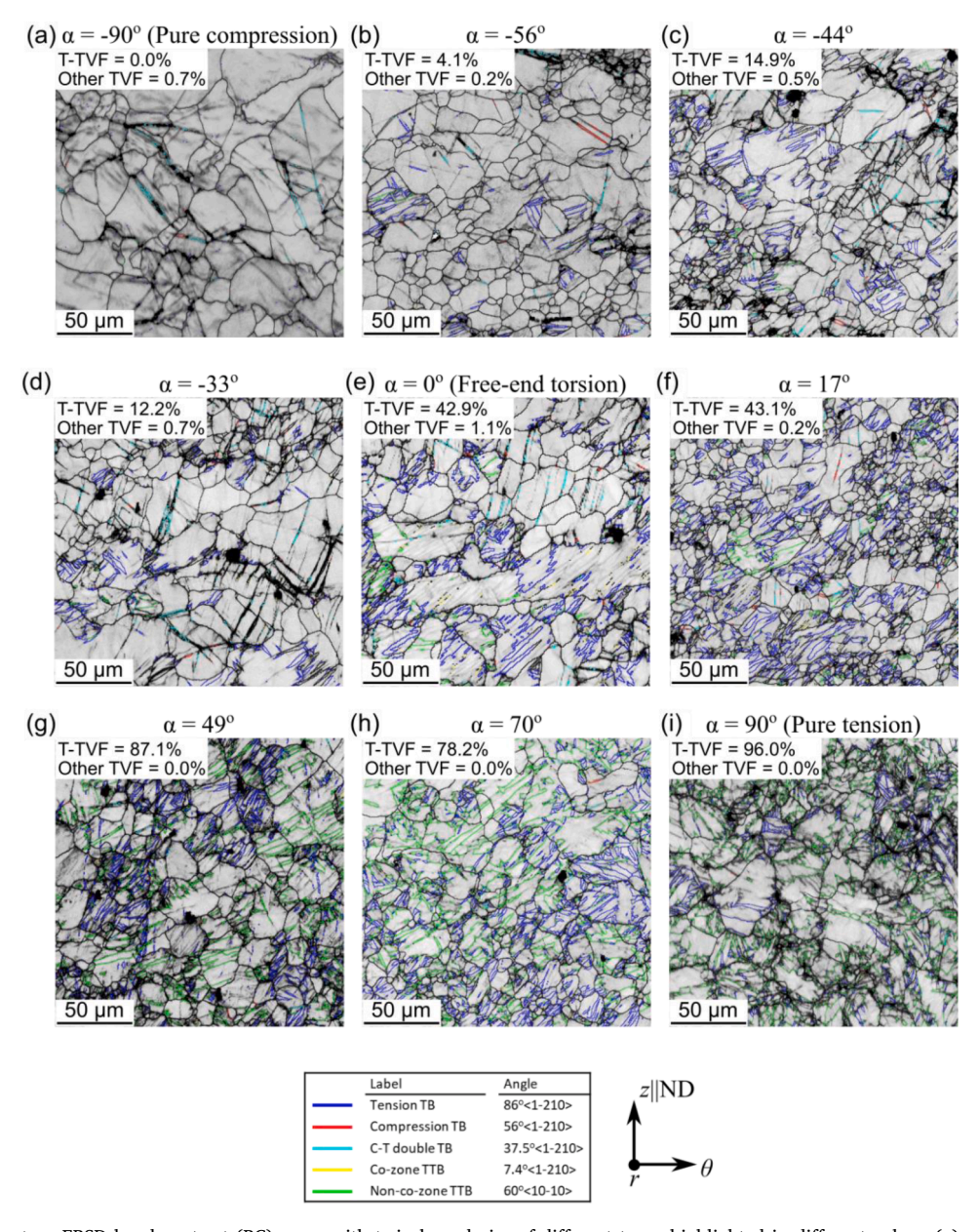


**Fig. 7.** Post-fracture EBSD band contrast (BC) maps with twin boundaries of different types highlighted in different colors: (a)  $\alpha = -90^{\circ}$  (pure compression); (b)  $\alpha = -56^{\circ}$ ; (c)  $\alpha = -44^{\circ}$ ; (d)  $\alpha = -33^{\circ}$ ; (e)  $\alpha = 0^{\circ}$  (free-end torsion); (f)  $\alpha = 17^{\circ}$ ; (g)  $\alpha = 49^{\circ}$ ; (h)  $\alpha = 70^{\circ}$ ; (i)  $\alpha = 90^{\circ}$  (pure tension).

basal slips and  $\langle c+a \rangle$  pyramidal slips contribute to the plastic strain up to final fracture (Xi et al., 2018). Since slips on  $\langle c+a \rangle$  pyramidal planes require a much higher activation stress due to its higher CRSS, a higher degree of material hardening is shown in the compression-torsion loading paths, as evidenced in Fig. 4. In addition to the hardening effect contributed by dislocation slips, the multiplication of twin boundaries and the energetically unfavorable formation of twin-twin boundaries may contribute to the hardening as well as to the increase of flow stress. A detailed analysis of the twinning structures under combined axial-shear stresses states is essentially important to understand the anisotropic response of textured Mg alloys, which will be discussed in the next section.

#### 3.3. Microstructure and texture after fracture

The post-fracture microstructure of AZ31B Mg alloy was analyzed by means of EBSD. The inverse pole figure (IPF) crystal orientation map and the corresponding (0001) pole figure for each of the nine loading paths are presented in Fig. 6.

Under monotonic compression ( $\alpha=-90^\circ$ ) (Fig. 6a), no significant change in the texture is observed because tension twinning is suppressed under compression along the ND. Some  $\{10\overline{1}1\}$  compression twins and  $\{10\overline{1}1\}-\{10\overline{1}2\}$  compression-tension twins of thin lenticular morphology are detected in a small fraction of the grains ( $\sim$ 0.7%). Under compression-torsion loading ( $\alpha=-56^\circ$ ,  $-44^\circ$ ,  $-33^\circ$ ) (Fig. 6b-d), thin  $\{10\overline{1}1\}$  and  $\{10\overline{1}1\}-\{10\overline{1}2\}$  twins are detected in a fewer fraction of the grains (<0.5%), while thicker  $\{10\overline{1}2\}$  tension twins can be found occupying a larger fraction of the grains (up to 15%). The texture at fracture under combined compression-torsion does not change significantly from the original texture due to the low twin volume fractions (TVFs) of the tension twins. Nevertheless, a slight change of texture can be detected for  $\alpha=-33^\circ$  where apparent intensities are observed near the edge of the (0001) pole figure at approximately  $20^\circ$  from the  $\theta$  (hoop)-direction (refer to Fig. 1 for the sample local coordinate system). Such a texture change caused by re-orientation of tension twinning can be viewed more clearly for free-end torsion ( $\alpha=0^\circ$ ) (Fig. 6e). Twinning under the pure shear stress state induces a distinct partial texture rotation on the  $z-\theta$  plane, causing the c-axes of twinned grains to remain almost perpendicular to the radial direction and located near the edge of the (0001) pole figure at approximately  $20^\circ$  from the  $\theta$ -direction. This explains why most of the observed twins have green ( $\overline{1210}$  direction) or blue ( $01\overline{10}$  direction) colors in the IPF maps.

Combined tension-torsion ( $\alpha=17^\circ$ ,  $49^\circ$ ,  $70^\circ$ ) generates multiple  $\{10\overline{1}2\}$  twin variants with distinct orientations with their colors close to green ( $\overline{1}2\overline{1}0$  direction), blue ( $01\overline{1}0$  direction), and red (0001 direction) in the IPF maps (Fig. 6f-h). The shear effect on the final texture is more pronounced for the torsion-dominated paths,  $\alpha=17^\circ$  and  $49^\circ$  (Fig. 6f, g), where the c-axes of most of the twinned grains are oriented at the edge of the (0001) pole figure at approximately  $20^\circ$  from the  $\theta$ -direction. In the tension-dominated loading path ( $\alpha=70^\circ$ ) (Fig. 6h), most of the grains are twinned because tension applied along the ND favors tension twinning. Consequently, the texture at fracture evolves closer to the case of pure tension (Fig. 6i) where the c-axes of the twinned grains are uniformly distributed on the  $r-\theta$  plane. However, it is observed that the pole intensities still show a slight rotation by  $20^\circ$  about the radial direction, which is due to the contributions of twin variants produced by the torsion component. Under pure tension ( $\alpha=90^\circ$ ), the final texture is characterized by the c-axes of the grains uniformly distributed on the  $r-\theta$  plane, i.e., most of (0001) pole intensities are distributed along the  $\theta$  axis of the pole figure (Fig. 6i).

The post-fracture EBSD band contrast (BC) maps with twin boundaries (TBs) of different types highlighted in different colors are presented in Fig. 7 for all the loading paths. The types of twin boundaries highlighted in the BC maps include primary tension TB

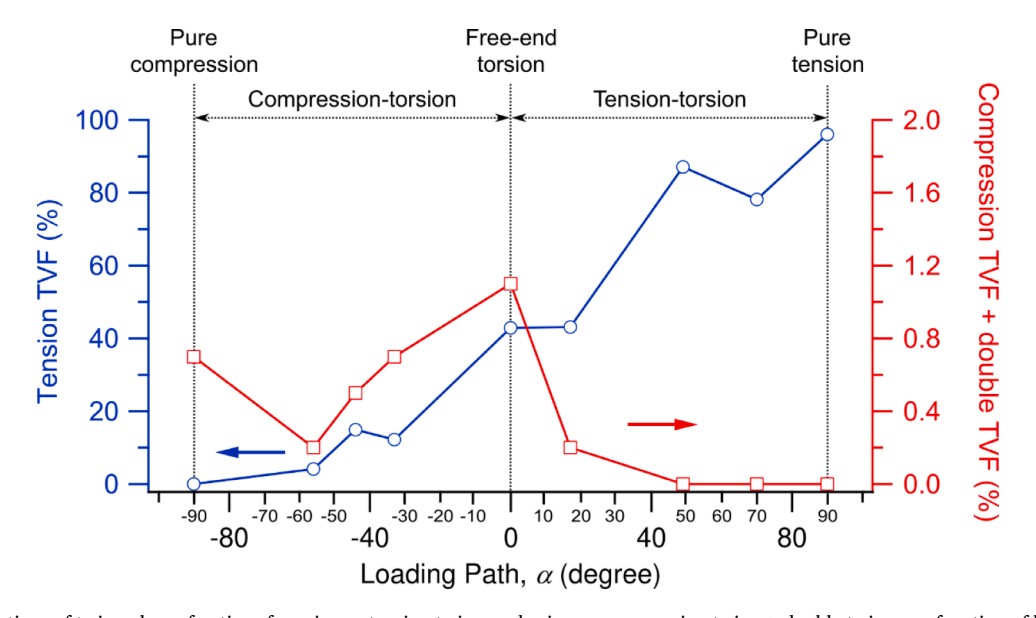


Fig. 8. Variations of twin volume fractions for primary tension twins, and primary compression twins + double twins as a function of loading path angle  $\alpha$ .

 $(86^\circ\pm5^\circ\langle1\overline{2}10\rangle)$ , blue), primary compression TB  $(56^\circ\pm5^\circ\langle1\overline{2}10\rangle)$ , red), and secondary compression-tension TB  $(37.5^\circ\pm5^\circ\langle1\overline{2}10\rangle)$ , cyan). The twin-twin boundaries (TTBs) are also highlighted, including non-co-zone TTB  $(60^\circ\pm5^\circ\langle10\overline{1}0\rangle)$ , yellow), and co-zone TTB  $(7.4^\circ\pm5^\circ\langle1\overline{2}10\rangle)$ , green). As can be inferred from the IPF maps in Fig. 6, most of the twins with thin lenticular morphology are identified as primary  $\{10\overline{1}1\}$  compression twins, or secondary  $\{10\overline{1}1\} - \{10\overline{1}2\}$  compression-tension double twins. Under compression loading  $(\alpha=-90^\circ)$  (Fig. 7a), all the detected twins are  $\{10\overline{1}1\} - \{10\overline{1}2\}$  compression-tension double twins. Under combined loading (Fig. 7b-f), boundaries of both compression and tension twins are detected for  $\alpha=-56^\circ$ ,  $-44^\circ$ ,  $-33^\circ$ ,  $0^\circ$ , and  $17^\circ$  When the loading path angle is higher than  $\alpha=49^\circ$ , tension TBs and TTBs are present. As the loading path angle  $\alpha$  increases, the profuse activation of multiple twin variants in a grain promotes the formation of twin-twin boundaries (yellow and green colors).

Fig. 8 presents the variations of twin volume fractions (TVFs) for primary  $\{10\overline{1}2\}$  tension twins, primary  $\{10\overline{1}1\}$  compression twins, and secondary  $\{10\overline{1}1\} - \{10\overline{1}2\}$  compression-tension double twins as a function of the loading path angle  $\alpha$ . The TVF was calculated as the ratio of the total area of a specific twin type to the total scanned area. The twin type was identified based on the twin boundary misorientation, as illustrated in Fig. 7. The tension TVF shows an overall increasing tendency with increasing loading path angle  $(\alpha)$ . A further analysis presented in Section 4.2 reveals that such behavior is attributed to the increase in the twin favorability with increasing  $\alpha$ , in terms of generalized Schmid factor. The volume fraction of the other twins, *i.e.*, compression + double twins initially decreases from 0.7% at  $\alpha=-90^\circ$  to 0.2% at  $\alpha=-56^\circ$ , then increases progressively to a maximum of 1.1% at  $\alpha=0^\circ$  Under tension-torsion paths, the compression + double TVF decreases at a fast rate to 0.2% at  $\alpha=17^\circ$  all the way down to zero at  $\alpha=49^\circ$ ,  $70^\circ$ , and  $90^\circ$  The unexpected initial decrease and subsequent increase of the compression and double TVFs when  $-90^\circ < \alpha < 0^\circ$  may be explained by the inhomogeneous deformation of Mg alloy under combined loading and the well-known non-SF formation of compression twins (Jonas et al., 2011). Such behavior indicates that the TVFs of primary compression and double twins may not be fully captured by using the Schmid criteria alone, as will be further discussed in Section 4.3.

#### 4. Further discussion

#### 4.1. Effect of stress state on strength and ductility

The equivalent fracture stress  $(\bar{c}_f)$ , which is a measure of the strength, and the equivalent fracture plastic strain  $(\bar{\epsilon}_{p,f})$ , which is a measure of ductility, are plotted as functions of the loading path angle  $(\alpha)$  in Fig. 9. This representation allows for a better visualization of the effect of the stress state on the strength and ductility of the rolled AZ31B Mg alloy. Overall, pure tension and pure compression result in the highest strength, and pure torsion with slight tension has the lowest strength. The ductility is inversely proportional to the strength: pure torsion results in the highest ductility and pure tension and pure compression have the lowest ductility. It is noticed that the minimum fracture stress does not occur at  $\alpha=0^\circ$  but at  $\alpha=17^\circ$  This may be attributed to the enhanced twinning favorability of tension-torsion loading due to the tensile axial stress, which will be discussed in Section 4.2.

The trends of strength and ductility shown in Fig. 9 indicate that relatively easier accommodation of the plastic deformation is achieved under the torsion-dominated loading paths than under the tension/compression-dominated loading paths. In the rolled texture, previous studies have shown that plastic deformation under pure torsion is mostly accommodated by <a>basal slips and

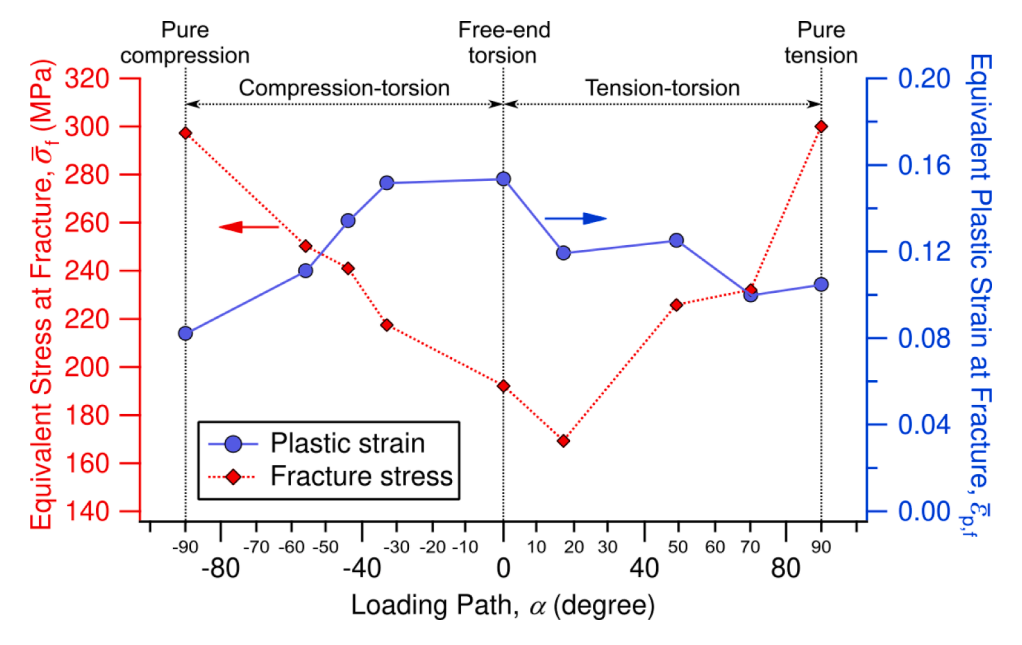


Fig. 9. Variations of equivalent fracture stress and equivalent plastic strain at fracture with the loading path angle.

tension twinning throughout the deformation (Carneiro et al., 2021b). On the other hand, deformation under monotonic compression is mostly accommodated by  $\langle a \rangle$  basal slips and  $\langle c+a \rangle$  pyramidal slip systems (Xi et al., 2018), whereas  $\langle a \rangle$  prismatic and  $\langle a \rangle$  basal slips are operated under monotonic tension at high strain levels (Carneiro et al., 2021b). As non-basal slips require higher CRSSs, the activation of these non-basal slips in the later stage under monotonic tension/compression may result in higher fracture stresses than under the tension/compression-dominated loading paths. For torsion-dominated loading paths, as deformation is mostly accommodated by basal slips and twinning with the attendance of non-basal slips to a lesser extent, the local stress levels are lowered which may result in a reduction of the strain incompatibility across the grains. This may lead to the enhanced ductility in the torsion-dominated loading paths. Similarly, Kim et al. (2012) reported an enhancement in ductility in an AZ31 Mg sheet under biaxial dome tests where basal and prismatic slips prevail without the presence of the hard-to-activate pyramidal slips. In short, the easy activation of basal slip systems and the limited activation of non-basal slips in the deformation involving shear stress state may be responsible for the higher ductility and lower fracture stress under the torsion-dominant loading paths.

#### 4.2. Schmid factor analysis for twinning favorability

In order to assess the twinning favorability under multiaxial stress state, a generalized Schmid Factor (SF) is calculated for a specific twin system in a grain using the crystal orientation obtained from the EBSD maps and considering the stress state. The generalized SF is the ratio of the resolved shear stress in a twin system to the externally applied von Mises equivalent stress (Xia et al., 2019),

$$SF = (b^t \cdot \sigma \cdot n)/\overline{\sigma} \tag{8}$$

where  $b^t$  is the normalized twin direction, n is the unit plane normal of the twin plane,  $\sigma$  is the applied stress tensor and  $\bar{\sigma}$  is the equivalent von Mises stress. Eq. (8) is applicable to a general stress state and offers an efficient way to compare the activation of a twin mode in grains with different crystal orientations in a polycrystal.

The twinning behavior of the AZ31B Mg alloy under different loading paths in the current study can be interpreted in terms of the

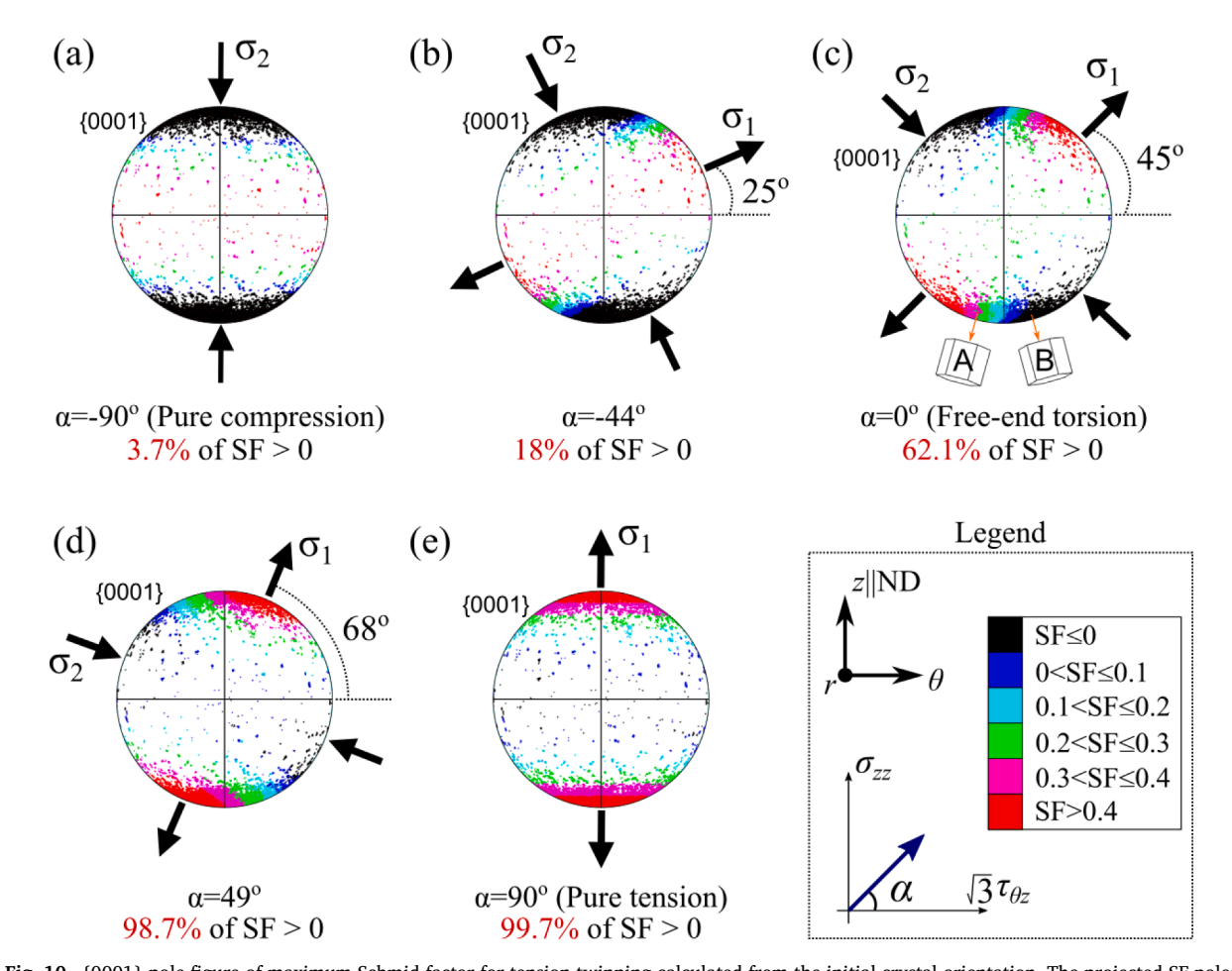
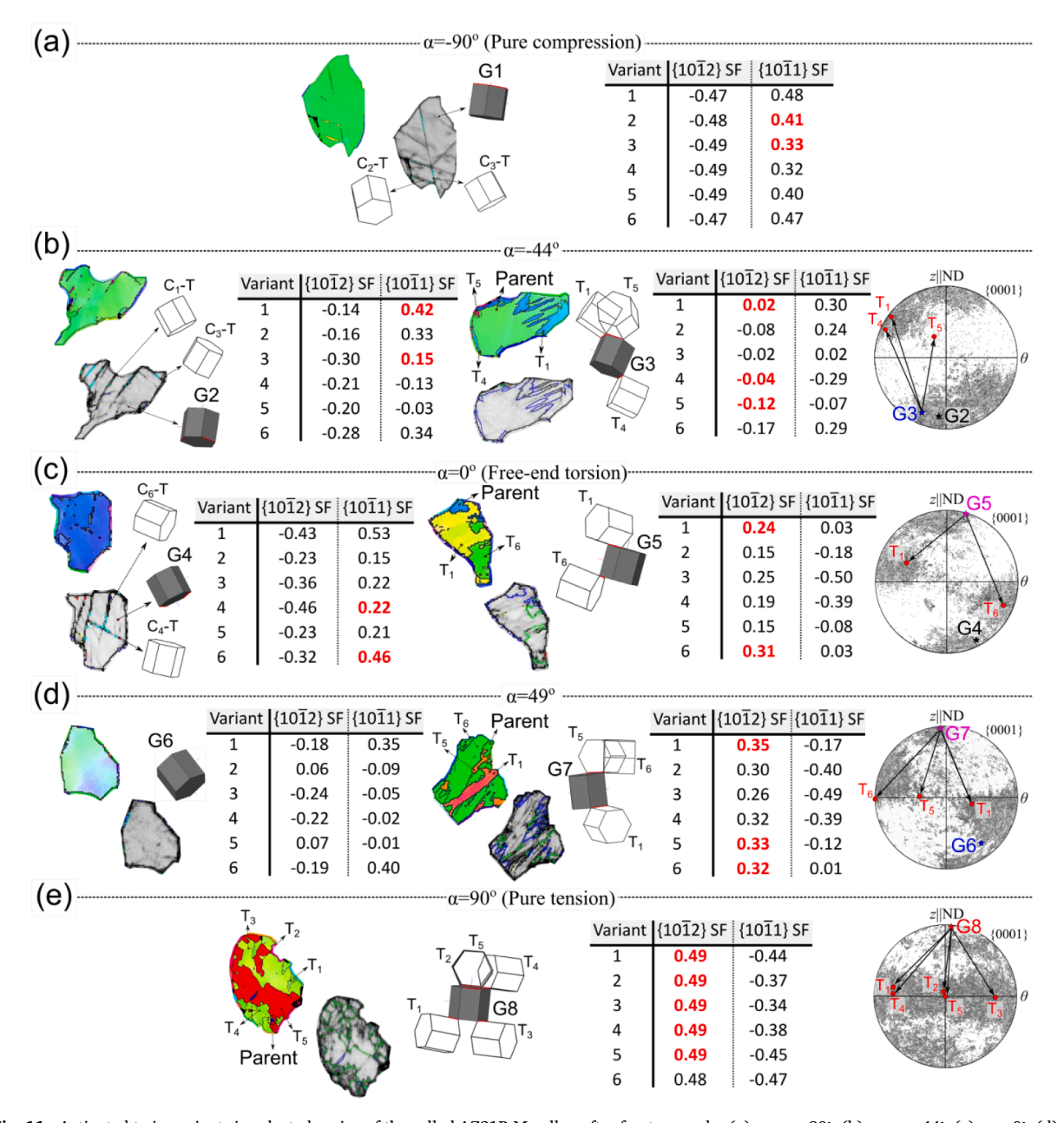


Fig. 10. {0001} pole figure of maximum Schmid factor for tension twinning calculated from the initial crystal orientation. The projected SF poles are colored according to different ranges of the maximum SF values.

influence of the stress state on the SF calculated based on the initial microstructure. Fig. 10 presents the generalized SF pole figures for tension twinning calculated for four representative loading paths. For each loading path, the theoretical maximum SFs for  $\{10\overline{1}2\}\langle10\overline{1}1\rangle$  tension twinning are calculated based on every crystal orientation scanned from the undeformed rolled AZ31B Mg alloy plate. The calculated SFs are projected in the (0001) pole figures (Fig. 10) according to the crystal orientation at each point. The directions of the applied principal stresses  $\sigma_1$  and  $\sigma_2$  for each loading case are also indicated in Fig. 10.

Under pure compression  $\alpha=-90^\circ$  (Fig. 10a), most of the grains have the *c*-axis parallel to the compression direction, resulting in negative SFs for tension twinning. With such a stress state, only 3.7% of the initial crystal orientations have positive SFs for tension twinning. Combined axial-torsion loading results in two none-zero principal stresses on the  $\theta-z$  plane, *i.e.*, tensile principal stress  $\sigma_1$  and compressive principal stress  $\sigma_2$  oriented perpendicular to each other. The angle between  $\sigma_1$  and the  $\theta$ -axis increases as the loading path angle  $\alpha$  increases. In these cases, the maximum SFs are observed on grains with *c*-axis parallel to the  $\sigma_1$  direction and, consequently, perpendicular to the  $\sigma_2$  direction. Therefore, the initial basal texture of the rolled AZ31B induces a higher favorability for



**Fig. 11.** Activated twin variants in selected grains of the rolled AZ31B Mg alloy after fracture under (a)  $\alpha = -90^{\circ}$ , (b)  $\alpha = -44^{\circ}$ , (c)  $\alpha = 0^{\circ}$ , (d)  $\alpha = 49^{\circ}$ , and (e)  $\alpha = 90^{\circ}$  The twin variants with a SF in red bold text are activated. (For interpretation of the references to colour in this figure legend, the reader is referred to the web version of this article.)

tension twinning as  $\alpha$  approaches 90°, i.e.,  $\sigma_1$  approaches  $z \parallel ND$ . For instance, under compression-torsion with  $\alpha = -44^\circ$  (Fig. 10b), the tensile principal stress  $\sigma_1$  forms an angle of 25° with the  $\theta$ -axis, resulting in 18% of the initial crystal orientations with positive SF values. Under free-end torsion,  $\alpha = 0^\circ$  (Fig. 10c), the angle between  $\sigma_1$  and  $\theta$  is 45°, and 62.1% of the grains are favorable for tension twinning. Under tension-torsion loading with  $\alpha = 49^\circ$ ,  $\sigma_1$  is oriented 68° towards  $\theta$ , and the fraction of grains favorable for tension twinning is 98.7%, as shown in Fig. 10d. The maximum favorability occurs under pure tension,  $\alpha = 90^\circ$ , where  $\sigma_1$  aligns with  $z \mid ND$  axis and 99.7% of the initial microstructure favors tension twinning.

The SF pole figures for tension twinning presented in Fig. 10 also indicate an asymmetric nature of the twinning favorability under combined axial-torsion loading. Since the principal stress  $\sigma_1$  is always oriented in the first and third quadrant of the (0001) pole figure, grains with c-axes misaligned by positive or negative rotations about the r-axis may induce twinning SFs of opposite signs. For instance, a grain misaligned 15° by negative rotation about r-axis, such as Grain A in Fig. 10c leads to a SF higher than 0.3, whereas a grain misaligned 15° by positive rotation about r-axis, such as Grain B results in a negative SF for tension twinning. These grains with negative SFs for tension twinning are favorable for compression twinning. Therefore, both tension twinning and compression twinning can occur under combined axial-torsion loading.

#### 4.3. Twin variant selection

Fig. 11 presents typical twin structures in selected grains depicted in Figs. 6-7. The SFs for all the six possible twin variants in the selected grains are also listed in the figure. The SFs for the selected twin variants are highlighted in red color. Symbols  $T_i$  (i = 1, 2, 3, ...6) represent the individual  $\{10\overline{1}2\}$  twin variants, following the label convention in (Yu et al., 2014) where  $T_1$  corresponds to the  $(10\overline{1}2)[\overline{1}011]$  variant, while increasing subscripts correspond to the other variants by a counter-clockwise rotation about the c-axis. Symbol  $C_i$  (i = 1, 2, 3, ...6) correspond to the  $\{10\overline{1}1\}$  compression twin variants, following the same labeling rule as for tension twinning. Secondary twins are represented by the individual twin types in the sequence of activation. For instance,  $C_i$ -T denotes a compression-tension double twin where a secondary tension twin T is formed inside the primary compression twin  $C_i$ .

Under pure compression,  $\alpha = -90^\circ$ , two compression-tension double twin variants ( $C_2$ -T and  $C_3$ -T) are activated in grain G1, as shown in Fig. 11a. It is noticeable that the selection of the primary compression twin variants does not strictly follow the Schmid law. For instance, variant  $C_1$  has the highest SF but it is not activated, while the activated variant is  $C_3$ , which has a SF with only the fifth highest rank. It has been reported that the activated primary compression twin variants in double twins usually have positive SFs in *hcp* metals (Xu et al., 2018). However, non-Schmid variant selection is also reported, which is related to the local stress state in the polycrystal Mg and possible defects responsible for twin nucleation (Mu et al., 2012). It has been shown that the activated primary variant is often the one that requires the least amount of activation energy to accommodate the strain from neighboring grains, such that the selected variant not necessarily has the highest SF hank (Jonas et al., 2011).

Unlike the cases of monotonic tension and monotonic compression, combined axial-torsion loading may induce the activation of either tension twins or compression twins depending on the specific grain orientation with respect to the stress state for a given texture. This is attributed to the twin favorability of a specific grain orientation with respect to the principal stresses, as represented in Fig. 10. For instance, under compression-torsion  $\alpha=-44^\circ$  (Fig. 11b), the orientation of grain G2 induces two compression-tension double twins (C<sub>1</sub>-T and C<sub>3</sub>-T), while the orientation of grain G3 induces three tension twin variants (T<sub>1</sub>, T<sub>4</sub>, and T<sub>5</sub>). Although compression twin variants detected in grain G3 have relatively high SFs (SF>0.15), it is noticed that tension twins may be activated with a low SF (SF for T<sub>1</sub> = 0.02) or even with negative SFs, such as T<sub>4</sub> and T<sub>5</sub> (SFs of -0.04 and -0.12, respectively), due to the much lower CRSS. Under free-end torsion  $\alpha=0^\circ$  (Fig. 11c), the orientation of grain G4 induces activation of two compression-tension double twins (C<sub>4</sub>-T and C<sub>6</sub>-T), while the orientation of G5 induces the activation of two tension twin variants (T<sub>1</sub> and T<sub>6</sub>) with high SFs of 0.31 and 0.24, respectively. Under tension-torsion  $\alpha=49^\circ$ , no compression twins are detected, even in the grains with high SFs for compression twin, such as grain G6 in Fig. 11d. This may occur due to the relatively low equivalent stress at fracture under  $\alpha=49^\circ$ , which reduces the resolved shear stress, and the high CRSS of compression twinning. Alternatively, most grains are favorable for tension twinning, such as grain G7, which is almost completely consumed by the three variants of the highest ranks T<sub>1</sub>, T<sub>5</sub>, and T<sub>6</sub>. Under pure tension,  $\alpha=90^\circ$ , most grains present high SF for tension twinning, such as grain G8 in Fig. 11e, which is completely consumed by T<sub>1</sub>, T<sub>2</sub>, T<sub>3</sub>, T<sub>4</sub>, and T<sub>5</sub>.

Overall, the observations in Figs. 11b-d show that the Schmid law can predict well the activation of primary tension twin variants for the given texture under combined axial-torsion loading at different paths. Therefore, the Schmid law may explain the distinct final twinning textures observed under combined axial-torsion loading, presented in Fig. 6c-h. The post-fracture twinning textures under combined loading and free-end torsion show two intensities located near the edge of the (0001) pole figure about 20° from the  $\theta$ -axis. This can be explained by the relationship between the twinning favorability and the direction of the principal stress  $\sigma_1$ , presented in Fig. 10, *i.e.*, grains with *c*-axes misaligned towards positive  $\theta$ -axis (first quadrant of the pole figures) are most favorable for tension twinning. Since tension twinning produces an 86° rotation of the crystal lattice, twinning in these non-ideally oriented crystals will reorient the *c*-axes not exactly on the  $r - \theta$  plane, but on a plane slightly tilted according to the angle of misorientation of the parent grain with the z|ND-axis. For instance, grain G5 in Fig. 11c has the *c*-axis misoriented by 15° from the z|ND-axis and the activated twin variants  $T_1$  and  $T_5$  have their *c*-axes oriented approximately 20° from  $\theta$ -axis. Furthermore, the twinning texture is concentrated at the edge of the (0001) pole figure due to the high SF ranks of twin variants that rotate the parent lattice about the *r*-axis within the  $z - \theta$  plane, instead of towards the *r*-axis. For instance,  $T_1$  in grain G3 (Fig. 11b), and  $T_6$  in grain G5 (Fig. 11c) have the highest SF ranks and rotate the parent grains almost within the  $z - \theta$  plane. The high SFs of these variants are induced by the compression direction

(Carneiro et al., 2021b; Hong et al., 2010; Park et al., 2010; Zhao et al., 2018).

#### 5. Conclusions

A rolled AZ31B Mg alloy was deformed monotonically under 10 combined axial-torsion loading paths ( $\alpha$ ):  $\alpha = -90^\circ$  (compression),  $-72^\circ$ ,  $-56^\circ$ ,  $-44^\circ$ ,  $-33^\circ$ ,  $0^\circ$  (free – end torsion),  $17^\circ$ ,  $49^\circ$ ,  $70^\circ$ , and  $90^\circ$  (tension). For each loading path, the post-fracture microstructure was characterized in terms of the twinning structures and the final deformation texture. The stress-strain responses and the microstructure as a function of the loading path were studied in detail with a focus on understanding the effect of the multiaxial stress state on the mechanical behavior and twinning structure of the rolled AZ31B. The following conclusions can be made.

- 1. The axial stress-axial plastic strain and the shear stress-shear plastic strain curves show a concave-down shape under compression-torsion loading paths ( $-90^{\circ} < \alpha < 0^{\circ}$ ) and a sigmoidal shape under tension-torsion loading paths ( $0^{\circ} \le \alpha < 90^{\circ}$ ). The sigmoidal shape becomes stronger as the loading path angle  $\alpha$  increases due to increased tension twinning.
- 2. At a given equivalent plastic strain under combined tension-torsion, the equivalent stress and plastic strain hardening capacity increases with increasing loading path angle  $\alpha$ . Under combined compression-torsion loading, the equivalent stress decreases and the equivalent plastic strain increases with increasing  $\alpha$ .
- 3. For the rolled Mg alloy under the combined axial-torsion loading, pure tension and pure compression have the maximum strength, torsion with slight tension results in the lowest strength, and the other combined loading paths fall in between for the strength. The dependence of the ductility on the loading path is opposite to that of the strength with the pure torsion producing the highest ductility.
- 4. The stress locus at fracture in the  $\sigma \sqrt{3}\tau$  space can be described well by an ellipse for the combined axial-torsion loading. The stress loci at equivalent plastic strains of 0.2% and 1.0% can also be described reasonably well by the ellipsis equations in the  $\sigma \sqrt{3}\tau$  space. However, for each equivalent plastic strain, two semi-ellipses with distinct major axes under tension-torsion and compression-torsion loading are needed.
- 5. Tension twinning is profuse under combined tension-torsion loading paths ( $0^{\circ} < \alpha < 90^{\circ}$ ), while both tension and compression twins are activated under combined compression-torsion loading ( $-90^{\circ} < \alpha < 0^{\circ}$ ). The tension twin volume fraction increases as  $\alpha$  increases, reaching a maximum of 96% under  $\alpha = 90^{\circ}$  (monotonic tension). The volume fraction of compression twins and compression-tension double twins increases when  $-90^{\circ} < \alpha < 0^{\circ}$  to a maximum of 1.1% when  $\alpha = 0^{\circ}$  and decreases to zero at  $\alpha > 49^{\circ}$
- 6. The primary tension twin variant selection follows the Schmid law reasonably well under combined loading, while the observed compression twin variants are not always those having Schmid factors with the maximum ranks.
- 7. The final twinning texture can be explained by the twin variant favorability according to the principal stress orientation under multiaxial stress state. In the rolled AZ31B Mg alloy texture, the activation of high Schmid factor (SF)-tension twin variants rotates the c-axis of parent grains towards the direction of the compressive principal stress  $\sigma_2$  in the  $z-\theta$  plane (the plane perpendicular to the radial direction of the tubular specimen). The high twinning favorability of grains with c-axes slightly misoriented from the longitudinal axis of the specimen (ND of the rolled plate) towards the direction of the tensile principal stress  $\sigma_1$  induces rotation of the basal poles to approximately 20° from the  $\theta$ -axis (circumferential direction of the tubular specimen).

### CRediT authorship contribution statement

Luiz Carneiro: Investigation, Methodology, Formal analysis, Writing – original draft. Qin Yu: Methodology, Writing – original draft. Yanyao Jiang: Conceptualization, Supervision, Project administration, Funding acquisition, Writing – review & editing.

#### **Declaration of Competing Interest**

The authors declare no competing financial interest.

#### Acknowledgments

The research was supported by the U.S. National Science Foundation (CMMI-1762312).

#### References

Abedini, A., Butcher, C., Worswick, M.J., 2018. Experimental fracture characterisation of an anisotropic magnesium alloy sheet in proportional and non-proportional loading conditions. Int. J. Solids Struct 144–145, 1–19.

Agnew, S.R., Duygulu, O., 2005. Plastic anisotropy and the role of non-basal slip in magnesium alloy AZ31B. Int. J. Plast. 21, 1161–1193.

Alkan, K., Aytuna, O.B., Güler, B., Efe, M., 2020. Strong strain path dependence of strain localizations and fracture in magnesium AZ31 sheet. J. Magnes. Alloy. 8, 472–479

Andar, M.O., Kuwabara, T., Steglich, D., 2012. Material modeling of AZ31 Mg sheet considering variation of r-values and asymmetry of the yield locus. Mater. Sci. Eng. A 549, 82–92.

Banabic, D., Hußnätter, W., 2009. Modeling the material behavior of magnesium alloy AZ31 using different yield criteria. Int. J. Adv. Manuf. Technol. 44, 969–976. Barnett, M.R., 2007a. Twinning and the ductility of magnesium alloys Part I. Tension Twins. Mater. Sci. Eng. A 464, 1–7. Barnett, M.R., 2007b. Twinning and the ductility of magnesium alloys. Part II. "Contraction" twins. Mater. Sci. Eng. A 464, 8–16.

- Carneiro, L., Culbertson, D., Yu, Q., Jiang, Y., 2021a. Twinning in rolled AZ31B magnesium alloy under free-end torsion. Mater. Sci. Eng. A 801, 140405.
- Carneiro, L., Culbertson, D., Zhu, X., Yu, Q., Jiang, Y., 2021b. Twinning characteristics in rolled AZ31B magnesium alloy under three stress states. Mater. Charact. 175, 111050.
- Cazacu, O., Barlat, F., 2004. A criterion for description of anisotropy and yield differential effects in pressure-insensitive metals. Int. J. Plast, 20, 2027-2045.
- Cheng, S., Krempl, E., 1991. Experimental determination of strain-induced anisotropy during nonproportional straining of an A1/Mg alloy at room temperature. Int. J. Plast. 7. 827–846.
- Cheng, Y., Fu, Y., Xin, Y., Chen, G., Wu, P., Huang, X., Liu, Q., 2020. {101-2} twinning behavior under biaxial tension of Mg-3Al-1Zn plate. Int. J. Plast. 132, 1–20. Chino, Y., Kimura, K., Mabuchi, M., 2009. Deformation characteristics at room temperature under biaxial tensile stress in textured AZ31 Mg alloy sheets. Acta Mater 57, 1476–1485.
- Dong, S., Yu, Q., Jiang, Y., Dong, J., Wang, F., Jin, L., Ding, W., 2017. Characteristic cyclic plastic deformation in ZK60 magnesium alloy. Int. J. Plast. 91, 25–47.
- Dorogoy, A., Rittel, D., Godinger, A., 2016. A Shear-Tension Specimen for Large Strain Testing. Exp. Mech. 56, 437-449.
- Dorogoy, A., Rittel, D., Godinger, A., 2015. Modification of the Shear-Compression Specimen for Large Strain Testing. Exp. Mech. 55, 1627-1639.
- Dorogoy, A., Rittel, D., Godinger, A., 2002. A Shear-compression Specimen for Large Strain Testing. Exp. Mech. 42, 58-64.
- Swift, H.W., 1947. Length Changes in Metals Under Torsional Overstrain. Engineering 163, 253.
- Hong, S.-.G., Park, S.H., Lee, C.S., 2010. Role of {10–12} twinning characteristics in the deformation behavior of a polycrystalline magnesium alloy. Acta Mater 58, 5873–5885.
- Iftikhar, C.M.A., Khan, A.S., 2021. The evolution of yield loci with finite plastic deformation along proportional and non-proportional loading paths in an annealed extruded AZ31 magnesium alloy. Int. J. Plast. 143, 103007.
- Inaba, T., Yoshikawa, T., Tokuda, M., 2008. Experimental study on deformation mechanism of AZ31 magnesium alloy under various temperature conditions. Int. J. Mod. Phys. B 22, 6233–6238.
- Jiang, J., Godfrey, A., Liu, W., Liu, Q., 2008. Microtexture evolution via deformation twinning and slip during compression of magnesium alloy AZ31. Mater. Sci. Eng. A 483–484, 576–579.
- Jiang, Lan, Jonas, J.J., Luo, A.A., Sachdev, A.K., Godet, S., 2007a. Influence of {10-12} extension twinning on the flow behavior of AZ31 Mg alloy. Mater. Sci. Eng. A 445-446. 302-309.
- Jiang, L., Jonas, J.J., Mishra, R.K., Luo, A.A., Sachdev, A.K., Godet, S., 2007b. Twinning and texture development in two Mg alloys subjected to loading along three different strain paths. Acta Mater 55, 3899–3910.
- Jonas, J.J., Mu, S., Al-Samman, T., Gottstein, G., Jiang, L., Martin, E., 2011. The role of strain accommodation during the variant selection of primary twins in magnesium. Acta Mater 59, 2046–2056.
- Kabirian, F., Khan, A.S., 2015. Anisotropic yield criteria in σ-τ Stress space for materials with yield asymmetry. Int. J. Solids Struct. 67-68, 116-126.
- Kelley, E.W., Hosford, W.F., 1968. Plane-strain compression of magnesium and magnesium alloy crystals. Trans. Metall. Soc. AIME 242, 5-13.
- Khan, A.S., Pandey, A., Gnäupel-herold, T., Mishra, R.K., 2011. Mechanical response and texture evolution of AZ31 alloy at large strains for different strain rates and temperatures. Int. J. Plast. 27, 688–706.
- Kim, H.L., Bang, W.K., Chang, Y.W., 2012. Effect of initial texture on deformation behavior of AZ31 magnesium alloy sheets under biaxial loading. Mater. Sci. Eng. A 552, 245–251.
- Knezevic, M., Levinson, A., Harris, R., Mishra, R.K., Doherty, R.D., Kalidindi, S.R., 2010. Deformation twinning in AZ31: influence on strain hardening and texture evolution. Acta Mater 58, 6230–6242.
- Kurukuri, S., Worswick, M.J., Tari, D.G., Mishra, R.K., Carter, J.T., 2014. Rate sensitivity and tension-compression asymmetry in AZ31B magnesium alloy sheet. Philos. Trans. R. Soc. A Math. Phys. Eng. Sci. 372, 20130216.
- Lamkanfi, E., Van Paepegem, W., Degrieck, J., Ramault, C., Makris, A., Van Hemelrijck, D., 2010. Strain distribution in cruciform specimens subjected to biaxial loading conditions. Part 1: two-dimensional *versus* three-dimensional finite element model. Polym. Test. 29, 7–13.
- Lou, X.Y., Li, M., Boger, R.K., Agnew, S.R., Wagoner, R.H., 2007. Hardening evolution of AZ31B Mg sheet. Int. J. Plast. 23, 44-86.
- Mohr, D., Chevin, M.A., Greve, L., 2013. Deformation behavior of magnesium extrusions with strong basal texture: experiments and modeling. J. Appl. Mech. Trans. ASME 80, 061002-1–14.
- Mu, S., Jonas, J.J., Gottstein, G., 2012. Variant selection of primary, secondary and tertiary twins in a deformed Mg alloy. Acta Mater 60, 2043-2053.
- Pan, H., Wang, F., Jin, L., Feng, M., Dong, J., 2016. Mechanical Behavior and Microstructure Evolution of a Rolled Magnesium Alloy AZ31B Under Low Stress Triaxiality. J. Mater. Sci. Technol. 32, 1282–1288.
- Park, S.H., Hong, S.G., Lee, C.S., 2010. Activation mode dependent {10-12} twinning characteristics in a polycrystalline magnesium alloy. Scr. Mater. 62, 202–205. Pollock, T.M., 2010. Weight loss with magnesium alloys. Science (80-.) 328, 986–987.
- Shi, B., Peng, Y., Yang, C., Pan, F., Cheng, R., Peng, Q., 2017. Loading path dependent distortional hardening of Mg alloys: experimental investigation and constitutive modeling. Int. J. Plast. 90. 76–95.
- Steglich, D., Jeong, Y., Andar, M.O., Kuwabara, T., 2012. Biaxial deformation behaviour of AZ31 magnesium alloy: crystal-plasticity- based prediction and experimental validation. Int. J. Solids Struct. 49, 3551–3561.
- Thomsen, E.G., Doen, J.E., 1944. The Effect of Combined Stresses on the Ductility and Rupture Strength of Magnesium-Alloy Extrusions. J. Aeronaut. Sci. 11, 125–136.
- Tomlinson, P., Azizi-Alizamini, H., Poole, W.J., Sinclair, C.W., Gharghouri, M.A., 2013. Biaxial deformation of the magnesium alloy AZ80. Metall. Mater. Trans. A 44, 2970–2983.
- Tucker, M.T., Horstemeyer, M.F., Gullett, P.M., El Kadiri, H., Whittington, W.R., 2009. Anisotropic effects on the strain rate dependence of a wrought magnesium alloy. Scr. Mater. 60, 182–185.
- Wang, H., Zhang, X., Wu, W., Liaw, P.K., An, K., Yu, Q., Wu, P., 2022. On the torsional and coupled torsion-tension/compression behavior of magnesium alloy solid rod: a crystal plasticity evaluation. Int. J. Plast. 151.
- Wang, Z., Qiu, J., Shu, X., Jin, T., 2020. Experimental study on the fracture behavior of AZ91D magnesium alloy under complex loading. Results Phys. 16, 102917. Wu, Z., Ahmad, R., Yin, B., Sandlobes, S., Curtin, W.A., 2018. Mechanistic origin and prediction of enhanced ductility in magnesium alloys. Science (80-.) 359, 447–452.
- Wu, Z., Curtin, W.A., 2015. The origins of high hardening and low ductility in magnesium. Nature 526, 62-67.
- Xi, B., Fang, G., Xu, S., 2018. Multiscale mechanical behavior and microstructure evolution of extruded magnesium alloy sheets: experimental and crystal plasticity analysis. Mater. Charact. 135, 115–123.
- Xia, D., Chen, X., Huang, G., Jiang, B., Tang, A., Yang, H., Gavras, S., Huang, Y., Hort, N., Pan, F., 2019. Calculation of Schmid factor in Mg alloys: influence of stress state. Scr. Mater. 171, 31–35.
- Xu, S., Gong, M., Jiang, Y., Schuman, C., Lecomte, J.-.S., Wang, J., 2018. Secondary twin variant selection in four types of double twins in titanium. Acta Mater 152, 58–76.
- Yang, B., Dong, Y., Guo, D., Yang, C., Zhang, X., Peng, Y., 2019. Anisotropic mechanical behavior and corresponding microstructure evolution of extruded AZ31 under combined normal /shear stress states. Mater. Sci. Eng. A 760, 415–425.
- Yoo, M.H., 1981. Slip, twinning, and fracture in hexagonal close-packed metals. Metall. Trans. A 12, 409-418.
- Yoshida, K., 2015. Prediction of ductile fracture induced by contraction twinning in AZ31 sheet subjected to uniaxial and biaxial stretching modes. Int. J. Plast. 84, 102–137.
- Yu, Q., Wang, J., Jiang, Y., McCabe, R.J., Li, N., Tomé, C.N., 2014. Twin-twin interactions in magnesium. Acta Mater 77, 28-42.
- Zhao, M., Kannan, V., Ramesh, K.T., 2018. The dynamic plasticity and dynamic failure of a magnesium alloy under multiaxial loading. Acta Mater 154, 124-136.